DOI:10.1002/ejic.201301080

Crystal and Magnetic Structure of Sr_2MIrO_6 (M = Ca, Mg) Double Perovskites – A Neutron Diffraction Study

Paula Kayser,*[a] María Jesús Martínez-Lope,[a] Jose Antonio Alonso,[a] María Retuerto,[b] Mark Croft,[c] Alexander Ignatov,[c] and Maria Teresa Fernández-Díaz[d]

Keywords: Iridium / Perovskite phases / Antiferromagnetic ordering / Magnetic properties / Spin–orbit coupling

---

Sr_2CaIrO_6 and Sr_2MgIrO_6 double perovskites have been prepared as polycrystalline powders from citrate precursors treated under oxygen pressure conditions. These compounds have been studied by X-ray and neutron powder diffraction (NPD), magnetic measurements, and X-ray absorption spectroscopy. The crystal symmetry of both oxides is monoclinic (space group $P2_1/n$), and the unit-cell parameters are related to the ideal simple perovskite cell as $a \approx \sqrt{2}a_0$, $b \approx \sqrt{2}a_0$, $c \approx 2a_0$, $\beta \approx 90°$, where a_0 is the edge of the simple cubic ABO_3 perovskite. This superstructure is a result of the 1:1 ordering of Ca/Mg and Ir ions over the B site and the distortion of the oxygen sublattice, which leads to a tilted three-dimensional network of corner-sharing BO_6 octahedra. Magnetic measurements indicate an antiferromagnetic ordering below T_N = 58 K for Sr_2CaIrO_6 and 74 K for Sr_2MgIrO_6. The low-temperature magnetic structure of Sr_2CaIrO_6 was determined by NPD and selected from the possible magnetic solutions compatible with the $P2_1/n$ space group according to the group-theory representation. The propagation vector is k = (1/2 1/2 0). A canted antiferromagnetic structure is observed below T_N with an ordered magnetic moment of 1.33(2) μ_B for the Ir^{6+} cations. Sr_2MgIrO_6 does not present magnetic reflections. An X-ray absorption spectroscopy investigation gives an insight into the Ir oxidation states and suggests a hexavalent state for the Ca compound and an admixture of Ir^{6+} and Ir^{5+} for the Mg perovskite, in agreement with the NPD data, which indicate a significant oxygen understoichiometry for this material.

Introduction

In recent years, the chemistry of mixed oxides containing 4d and 5d transition-metal cations has attracted a great deal of attention, as they present a wide variety of structures and exhibit interesting electronic and magnetic properties.[1] The increased spatial extent of the 4d/5d orbitals of the second/third-row transition-metal ions, with respect to the rather localized 3d orbitals of the first-row transition-metal ions, gives rise to weaker Coulomb interactions. This leads to a greater level of splitting in the crystal field and a consequent increase of the sensitivity of these ions to lattice distortions, especially in layered oxides such as Sr_2RuO_4, Sr_2RhO_4, Sr_2IrO_4,[2] and $NaIrO_3$.[3] Moreover, the spin–orbit coupling effect has to be considered in those compounds containing 4d and 5d transition metals,[4] as the characteristic energy of the spin–orbit coupling approaches that of the Coulomb interactions; this modifies the relative energy scale and, thus, the appearance of new phases with unusual electronic structures is expected.

Iridium-based perovskite or perovskite-like oxides are considerably less explored, although they are expected to exhibit interesting physical properties. The ability of Ir to exist in different oxidation states and its more extended 5d orbitals, together with the spin–orbit coupling, result in a rich variety of possibilities. Although Ir^{4+} is the most common oxidation state, Ir^{3+} has been described in the octahedral site of double perovskites such as Sr_2TaIrO_6 and Sr_2NbIrO_6;[5] Ir^{5+} and Ir^{6+} can also be obtained under high oxygen pressure conditions. The stabilization of Ir^{5+} and Ir^{6+} is especially interesting because the Ir^{5+}–O and Ir^{6+}–O bonds should be among the strongest chemical bonds in an oxygen lattice. The covalency of such chemical bonding correlates with the magnetic-ordering temperatures. For instance, Sr_2CrIrO_6 is expected to present the highest T_C among the double perovskites.[6] All these aspects were also discussed by Demazeau et al. in their pioneering work related to iridium double perovskites. In particular, Sr_2CaIrO_6 and Sr_2MgIrO_6 were first described by Demazeau et al.[7–9] and they determined their crystal structures by X-ray diffraction as monoclinic and cubic, respectively.

---

[a] Instituto de Ciencia de Materiales de Madrid, C.S.I.C.,
Cantoblanco, 28049 Madrid, Spain
E-mail: paula.kayser@icmm.csic.es
http://www.icmm.csic.es/
[b] Department of Chemistry and Chemical Biology, Rutgers, The State University of New Jersey,
610 Taylor Road Piscataway, NJ 08854-808, USA
[c] Department of Physics and Astronomy, Rutgers, The State University of New Jersey,
610 Taylor Road Piscataway, NJ 08854-808, USA
[d] Institut Laue-Langevin,
BP 156X, 38042 Grenoble, France

Supporting information for this article is available on the WWW under http://dx.doi.org/10.1002/ejic.201301080.

Subsequently, there have been exploratory studies on the $Sr_2Ir_{2-x}M_xO_6$ solid solutions;[10–12] in particular, $SrIr_{1-x}Mg_xO_3$ (x = 0.20 and 0.33) have been described to crystallize in the orthorhombic *Pbnm* space group and to show ferromagnetic properties.

The purpose of the present work is threefold: (1) we revisit the crystal structures of both perovskites from high-resolution neutron powder diffraction (NPD) data; we show that the symmetry for both perovskites is compatible with the $P2_1/n$ space group; (2) in addition, we report on the magnetism and the magnetic structure from low-temperature NPD data, and (3) we describe the results of an X-ray absorption spectroscopy investigation, which gives an insight into the Ir oxidation states.

Results and Discussion

Crystal Structures

Sr_2CaIrO_6 and Sr_2MgIrO_6 compounds were obtained as well-crystallized powders. The XRD patterns, shown in Figure 1, are characteristic of a perovskite structure and exhibit superstructure peaks corresponding to the $Ca^{2+}/Mg^{2+}–Ir^{6+}$ ordering. Both diagrams are indexed in a monoclinic cell ($P2_1/n$ space group). The cell parameters are related to a_0 (ideal cubic perovskite $a_0 \approx 3.8$ Å) as $a \approx \sqrt{2}a_0$, $b \approx \sqrt{2}a_0$, $c \approx 2a_0$, $\beta \approx 90°$.

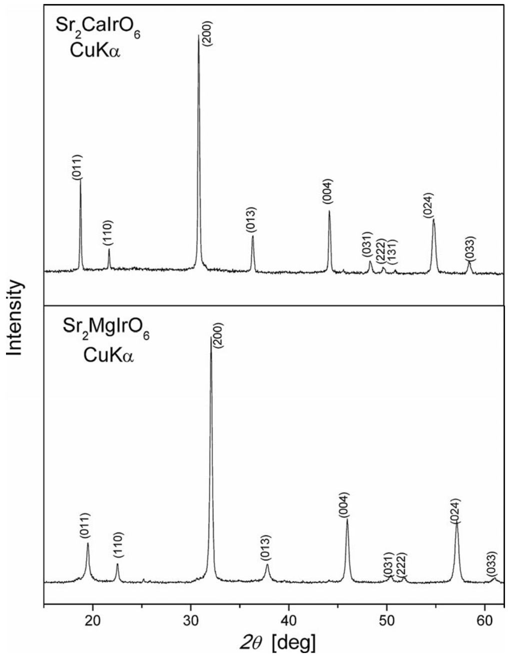

Figure 1. XRD patterns (Cu-K_α, λ = 1.5406 Å) for Sr_2MIrO_6 (M = Ca, Mg).

The crystal-structure refinement was performed from high-resolution NPD data by using the monoclinic $P2_1/n$ (no. 14) space group previously considered by Demazeau et al.[7] In this model, the Sr atoms are located at 4e (x, y, z) positions, the Ca/Mg atoms are at 2d (1/2, 0, 0) positions, the Ir atom are at 2c (1/2, 0, 1/2), and the O atoms are at 4e (x, y, z) sites. The Rietveld analysis resulted in a satisfactory agreement between the observed and calculated profiles (Figure 2). In this former model, the Ca/Mg and Ir ions are placed at two different B sites with a rock-salt ordered arrangement. As a second step, the possibility of antisite disordering was checked by allowing some Ca/Mg atoms to occupy Ir sites and vice versa. The refinement of the inversion degree led to 5% antisite disordering for the Ca compound and 20% for the Mg compound. The oxygen content was also examined; the occupancy factor of oxygen atoms was refined, and the result confirms a full stoichiometry for the Sr_2CaIrO_6 sample and the presence of oxygen vacancies for $Sr_2MgIrO_{6-\delta}$ [δ = 0.11(1)] at O2 positions. The remaining oxygen sites converged to values slightly higher than one and then were fixed to unity. Table 1 lists the most important atomic parameters of the structural refinement, and some selected room-temperature bond lengths and angles are included in Table 2.

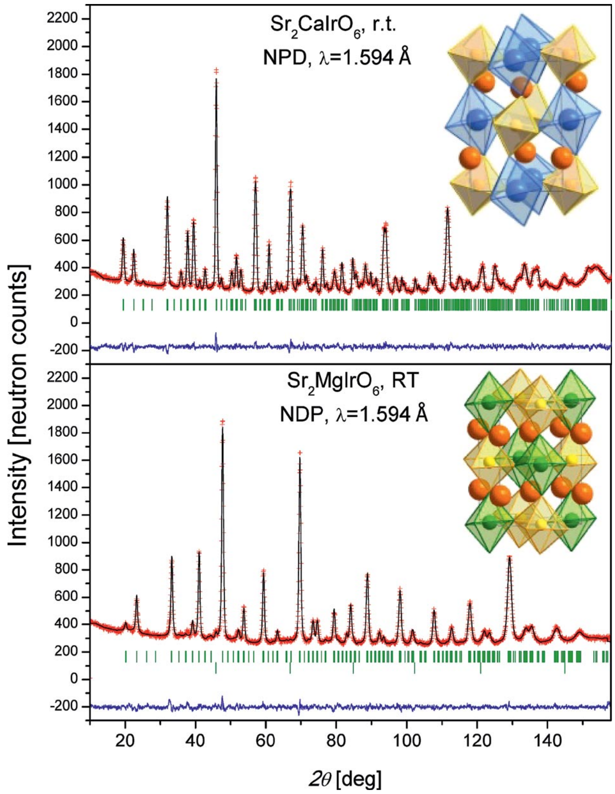

Figure 2. Observed (crosses), calculated (solid line), and difference (bottom) NPD Rietveld profiles for Sr_2MIrO_6 (M = Ca, Mg) at room temp. collected at the high flux D2B-ILL diffractometer. The first series of Bragg reflections corresponds to the main perovskite phase, and the second corresponds to vanadium from the sample holder. The inset shows a schematic representation of the monoclinic crystal structures, which involve a 1:1 long-range ordering of M and Ir atoms.

In the Sr_2MgIrO_6 perovskite, the smaller size of the Mg^{2+} ($^{VI}r_{Mg2+}$ = 0.72 Å) cation, with respect to that of Ca^{2+} ($^{VI}r_{Ca2+}$ = 1.00 Å), corresponding to the tolerance factors of $t_{Sr_2CaIrO_6}$ = 0.92 and $t_{Sr_2MgIrO_6}$ = 0.98, would suggest a structure with higher symmetry (tetragonal or cubic) at room temperature. Although the Rietveld analysis with a

Table 1. Unit-cell, positional, and thermal parameters for Sr_2MIrO_6 (M = Ca, Mg) defined in the monoclinic $P2_1/n$ (no. 14) space group, $Z = 2$, from NPD data at room temp.

	Sr_2CaIrO_6	Sr_2MgIrO_6
a [Å]	5.7668(2)	5.5909(8)
b [Å]	5.8160(2)	5.5754(6)
c [Å]	8.1766(3)	7.8839(8)
β [°]	89.7208/(2)	89.906(1)
V [Å^3]	274.24(2)	245.75(5)
Sr 4e (x, y, z)		
x	0.9932(6)	1.005(3)
y	0.0367(3)	–0.004(3)
z	0.2492(5)	0.249(2)
B [Å^2]	0.798(6)	1.15(2)
(Ca/Mg) 2d (1/2, 0, 0)		
Occ. $(Ca\text{-}Mg/Ir)_{2d}$	0.95(2)/0.05(2)	0.796/0.204
B [Å^2]	0.89(1)	0.47(2)
Ir 2c (1/2, 0, 1/2)		
Occ $(Ir/Ca\text{-}Mg)_{2c}$	0.95(2)/0.05(2)	0.796/0.204
B [Å^2]	0.208(6)	0.47(2)
O1 4e (x, y, z)		
x	0.0712(5)	0.023(1)
y	0.4790(6)	0.492(3)
z	0.2299(4)	0.246(2)
Occ (O1)	1.0	1.0
B [Å^2]	0.89(1)	0.61(8)
O2 4e (x, y, z)		
x	0.7310(6)	0.752(2)
y	0.3073(5)	0.252(3)
z	0.0380(5)	0.018(2)
Occ (O2)	1.0	0.947(6)
B [Å^2]	0.88(1)	1.16(8)
O3 4e (x, y, z)		
x	0.1908(6)	0.217(2)
y	0.2291(7)	0.226(3)
z	0.9589(4)	0.969(1)
Occ (O3)	1.0	1.0
B [Å^2]	0.85(1)	1.47(9)
Reliability Factors		
$\chi 2$	1.66	1.55
R_p [%]	2.58	2.31
R_{wp} [%]	3.21	2.96
R_{exp} [%]	2.50	2.38
R_I [%]	3.92	1.90

Table 2. Main interatomic bond lengths [Å] and selected angles [°] for Sr_2MIrO_6 (M = Ca, Mg) determined from NPD data at room temp.

Sr_2CaIrO_6		Sr_2MgIrO_6	
SrO polyhedra			
Sr–O1	2.616(4)	Sr–O1	2.81(2)
Sr–O1	2.541(5)	Sr–O1	2.77(2)
Sr–O2	2.788(5)	Sr–O1	2.954(20)
Sr–O2	2.541(5)	Sr–O1	2.637(20)
Sr–O2	2.883(5)	Sr–O2	2.71(2)
Sr–O3	2.856(5)	Sr–O2	2.70(2)
Sr–O3	2.535(5)	Sr–O2	2.86(2)
Sr–O3	2.794(5)	Sr–O2	2.90(2)
<Sr–O>	2.694(5)	Sr–O3	2.81(2)
		Sr–O3	3.10(2)
		Sr–O3	2.46(2)
		Sr–O3	2.83(2)
		$\langle Sr\text{–}O\rangle_{8short}$	2.716(20)
$(Ca/Mg)O_6$ polyhedra			
Ca–O1 (×2)	2.248(3)	Mg–O1 (×2)	2.009(12)
Ca–O2 (×2)	2.252(4)	Mg–O2 (×2)	1.995(14)
Ca–O3 (×2)	2.252(4)	Mg–O3 (×2)	2.038(13)
<Ca–O>	2.251(4)	<Mg–O>	2.014(13)
IrO_6 polyhedra			
Ir–O1 (×2)	1.930(3)	Ir–O1 (×2)	1.943(12)
Ir–O2 (×2)	1.938(3)	Ir–O2 (×2)	1.963(14)
Ir–O3 (×2)	1.950(4)	Ir–O3 (×2)	1.966(15)
<Ir–O>	1.939(3)	<Ir–O>	1.957(14)
Ca–O1–Ir	156.2(1)	Mg–O1–Ir	172.0(5)
ϕ	11.9	ϕ	4.0
Ca–O2–Ir	155.6(1)	Mg–O2–Ir	171.8(6)
ϕ	12.2	ϕ	4.1
Ca–O3–Ir	153.9(1)	Mg–O3–Ir	160.9(6)
ϕ	13.0	ϕ	9.5

tetragonal unit cell ($I4/m$ space group), in which the Sr atoms are placed at 4d (0, 1/2, 1/4) positions, the Mg atoms are placed at 2a (0, 0, 0), the Ir atoms are placed at 2b (0, 0, 1/2) positions, and the O atoms are placed at 4e (0, 0, z) and 8h (x, y, 0) sites, shows a reasonable agreement between the observed and calculated pattern, at high diffraction angles some unjustifiable reflections are noticeable (Figure S1). This confirms that the Sr_2MgIrO_6 perovskite crystallizes in the $P2_1/n$ space group. This splitting also discards the option of the cubic space group ($Fm\bar{3}m$) reported by Demazeau et al. for Sr_2MgIrO_6.[7]

The unit-cell parameters, listed in Table 1, correlate with the size of the alkaline-earth ions Ca and Mg, for instance, the unit-cell volumes are V = 274.24(2) and 245.75(5) Å^3. In the same way, in Sr_2CaIrO_6, the monoclinic distortion is more pronounced than in Sr_2MgIrO_6, and the monoclinic β angles are 89.7208(2) and 89.906(1)°, respectively; in both cases, this angle is very close to 90°, and a and b are very similar, which indicates a strong pseudotetragonal symmetry. In both compounds, the SrO polyhedron is reduced to an eightfold coordination owing to the tilting of the MO_6 octahedra. The average Sr–O bond lengths of 2.694(5) and 2.716(20) Å for Sr_2CaIrO_6 and Sr_2MgIrO_6, respectively, are in reasonable agreement with that expected from ionic radii sums of 2.66 Å for $^{VIII}Sr^{2+}$ (1.26 Å) and $^{VI}O^{2-}$ (1.40 Å).[13] The average interatomic distances in the $(Ca/Mg)O_6$ polyhedron [2.251(4) and 2.014(13) Å for the Ca and Mg compounds, respectively] are slightly shorter than those expected from the sums of the Shannon[13] effective radii of 2.40 and 2.12 Å ($^{VI}Ca^{2+}$ = 1.00 Å, $^{VI}Mg^{2+}$ = 0.72 Å and $^{VI}O^{2-}$ = 1.40 Å), which indicates that the Ca^{2+}/Mg^{2+}cations are overbonded and under compressive stress. On the other hand, the <Ir–O> distance [1.939(9) Å] in the Sr_2CaIrO_6 perovskite is somewhat longer than that in the same compound reported by Demazeau et al. (1.92 Å).[7] From their structural data, they gave an Ir^{6+} ionic radius of 0.52 Å. On the other hand, in Sr_2MgIrO_6, the average Ir–O bond length [1.957(14) Å] is even longer in spite of the smaller unit-cell parameters; this suggests the presence of some Ir^{5+} ions (0.57 Å), which are larger than Ir^{6+} ions, owing to the oxygen understoichiometry found in $Sr_2MgIrO_{5.89(1)}$. Another effect to take into account in the distances is the nonnegligible antisite disorder, more prominent in the case of Mg (ca. 20%). This disorder affects the observed over- and underbonding of Mg–O and Ir–O distances, respectively; as Ir^{6+} ions are partially introduced into Mg^{2+} sites, the average Mg–O distances decrease and vice versa. In the case of Ca, we only observe 5% of disorder; however, the difference in size between the Ca^{2+} and Ir^{6+} ions is larger than in the case of Mg, so we believe the disorder could also be the responsible for the over- and underbonding observed.

In the CaO_6, MgO_6, and IrO_6 octahedra, the three distances Ca/Mg–O and Ir–O are identical within error, which implies that there is a regular oxygen environment for the Ca^{2+}/Mg^{2+} and $Ir^{6+/5+}$ cations. As a measure of the octahedral distortion, the relationship between the largest B–O bond $(d\text{B–O})_L$ and the shortest one $(d\text{B–O})_S$ can be calculated. For Sr_2CaIrO_6, the calculated values are 1.002 for CaO_6 and 1.01 for IrO_6, and for the Mg-containing compound, this ratio is 1.02 for both octahedra. In addition, the O–Ca/Mg–O and O–Ir–O bond angles are all virtually 90°; thus, all of them are quasiregular octahedra.

To optimize the Sr–O bond lengths, the $(Ca/Mg)O_6$ and IrO_6 octahedra are forced to tilt. The average tilt angles can be estimated as $\phi = (180 - \omega)/2$, where ω is the Ca/Mg–O–Ir bond angle (Table 2). The monoclinic structure contains alternating $(Ca/Mg)O_6$ and IrO_6 octahedra tilted in antiphase along the (100) and (010) directions of the pseudocubic cell and tilted in phase along the (001) direction, as corresponds to the $a^-a^-c^+$ Glazer notation for Sr_2CaIrO_6 and Sr_2MgIrO_6, derived by Woodward et al.[14]

It is interesting to compare Sr_2MgIrO_6 with the previously reported $SrIr_{1-x}Mg_xO_3$ ($x = 0.20$ and 0.33) series.[10] In $SrIr_{1-x}Mg_xO_3$, the amount of Mg is not large enough to establish long-range order over the B site, and these compounds are described with orthorhombic symmetry. In contrast, Sr_2MgIrO_6 exhibits rock-salt order and crystallizes in the monoclinic $P2_1/n$ space group. The internal parameters are directly affected by the oxidation state of the iridium cation. Contrary to expectations, considering the greater ionic radii of the Mg cations with respect to the Ir cations, the volumes of the $SrIr_{1-x}Mg_xO_3$ phases are larger than the corresponding volume of Sr_2MgIrO_6, which suggests that the cell expansion is related to the presence of $Ir^{4+/5+}$ ions instead of Ir^{6+} ions.

Magnetic Properties

Figure 3 displays the molar magnetic susceptibility versus temperature curves of Sr_2CaIrO_6 and Sr_2MgIrO_6. Transitions to antiferromagnetic orderings are observed with Néel temperatures (T_N) of ca. 58 and 74 K, respectively. The magnetization versus magnetic field curves for both samples, measured at 4, 50, and 300 K (Figure 4), present an almost linear response with no hysteresis or remanent magnetization. The shapes of the curves at low temperatures exhibit the characteristic behavior of antiferromagnetic materials.

In the paramagnetic region, the inverse molar susceptibility versus temperature curves of each compound follow the Curie–Weiss law. The Curie constant and the Weiss temperature estimated from the fits are shown in the inset of Figure 3. The negative values of θ_W [$\theta_{W(Sr_2CaIrO_6)} = -363.4(5)$ K and $\theta_{W(Sr_2MgIrO_6)} = -418(1)$ K] suggest that the main magnetic interactions are antiferromagnetic. Effective magnetic moments (μ_{eff}) of 3.43 and 2.12 μ_B for Sr_2CaIrO_6 and Sr_2MgIrO_6, respectively, obtained from the Curie constants, indicate the presence of Ir with lower oxidation state in the Mg compound. As the effective magnetic moment of Ir^{6+} ions, experimentally obtained, is rather close to the spin-only value ($S = 3/2$ $\mu_{cal} = 3.87\,\mu_B$) in Sr_2CaIrO_6, the

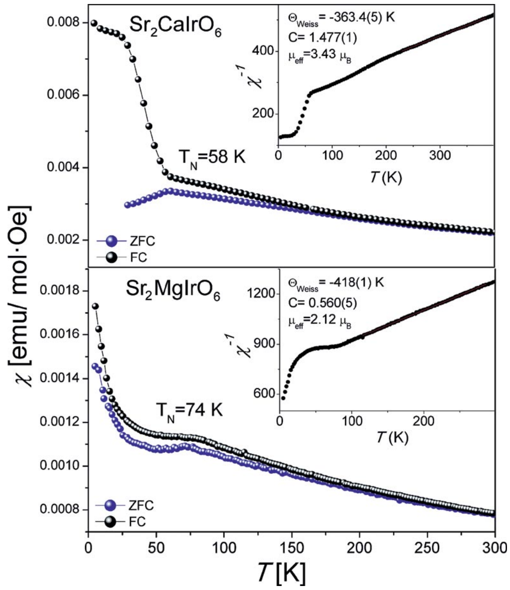

Figure 3. Temperature dependence of the direct current (dc) magnetic susceptibility for the Sr_2MIrO_6 (M = Ca, Mg) perovskites measured under a 0.1 T magnetic field. The inset shows the reciprocal susceptibility vs. temperature.

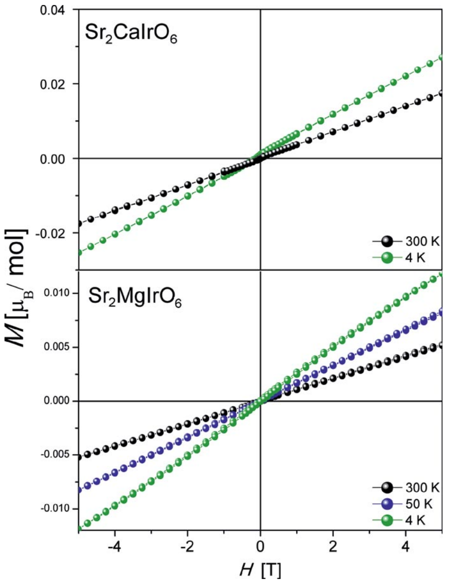

Figure 4. Magnetization vs. magnetic field isotherms at 4 and 300 K for Sr_2CaIrO_6 and at 4, 50, and 300 K for Sr_2MgIrO_6 measured under a magnetic field ranging from –5 to 5 T.

spin–orbit coupling characteristic of the 5d metal transition is then not observed on the Ir^{6+} magnetic moment value. In Sr_2MgIrO_6, the discrepancy between the experimental and the calculated magnetic moment values is larger, and the reduced moment suggests the presence of Ir^{5+} ions (this ion has been described as nonmagnetic in previous work)[1,15–18] or perhaps the presence of short-range correlations in the high-temperature region in which the Curie–Weiss law has been applied.

A typical feature of geometrically frustrated materials is the divergence in the zero-field-cooled (ZFC) and field-cooled (FC) curves at low temperature. We observe such divergence in both compounds, although it is more pronounced in Sr_2CaIrO_6, at temperatures much higher than the transition temperature; this again suggests the presence of magnetic correlations, probably short-range interactions, at temperatures above the magnetic-order temperature. Frustration effects in the magnetic cell are linked to different types of magnetic interactions or geometrical frustrations and give rise to spin-glass behavior in some materials.

Magnetic Structure

The low-temperature magnetic structure has been determined from the Rietveld analyses of the NPD diagrams collected at 2 K with the D1B instrument for Sr_2CaIrO_6 and Sr_2MgIrO_6. With respect to the room-temperature pattern (Figure 2), the 2 K neutron pattern of Sr_2CaIrO_6 shows weak low-angle reflections, which are forbidden for the crystallographic Bragg reflections and indicate a long-range antiferromagnetic ordering. To study the temperature dependence of the magnetic peaks, the thermal evolution of the NPD patterns, sequentially acquired upon cooling, was followed in the temperature range 2–100 K (Figure 5, a). At 50 K, the intensity of some magnetic reflections regularly increases as the temperature decreases and this corresponds to the antiferromagnetic ordering of the Ir^{6+} moments. The ordered magnetic temperature agrees with the Néel temperature obtained from the magnetic measurements.

For Sr_2CaIrO_6, the magnetic peaks could be indexed with the propagation vector k = (1/2 1/2 0). After checking all of the possible magnetic modes compatible with the space-group symmetry and the propagation vector, the best agreement with the experimental data was obtained for the magnetic structure given by the basis vectors of the irreducible representation Γ_4: the two magnetic atoms present in the unit cell, Ir1 at (1/2 0 1/2) and Ir2 at (0 1/2 0), are magnetically coupled as $m_{1x} = -m_{2x}$ and $m_{1z} = -m_{2z}$. This magnetic arrangement leads to a good agreement between the observed and calculated magnetic intensities. Figure 6 shows the final Rietveld plot including the crystallographic phase and the magnetic phase. The refined components of the magnetic moment along the crystallographic axes are $m_x = 0.4(2)\ \mu_B$ and $m_z = 1.27(7)\ \mu_B$, and the net moment has a value of $1.33(2)\ \mu_B$. As shown in Figure 7, the magnetic structure consists of antiferromagnetic [011] layers of Ir^{6+} moments coupled antiferromagnetically with the spins directed approximately along the c axis interleaved with Ca layers. The reduction of the ordered magnetic moment [$1.33(2)\ \mu_B$] with respect to that expected for a t_{2g}^3 configuration of $3\ \mu_B$ is probably related to the divergence of the ZFC and FC curves and suggests that the presence of irre-

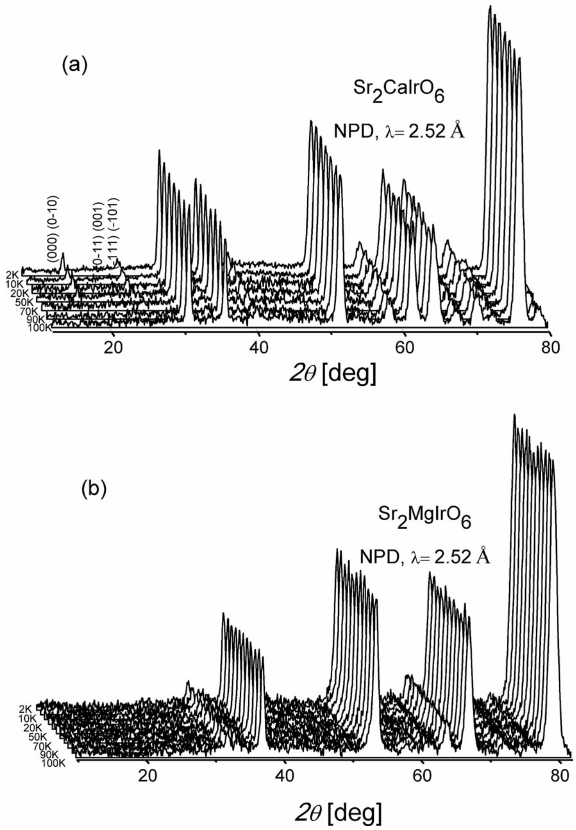

Figure 5. Thermal evolution of the NPD patterns of (a) Sr_2CaIrO_6 and (b) Sr_2MgIrO_6 acquired with λ = 2.52 Å in the temperature interval $2 < T < 100$ K.

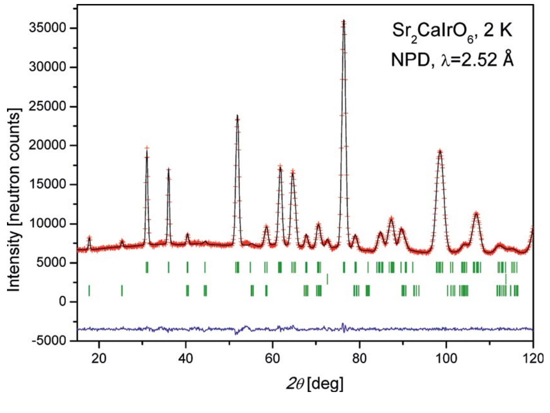

Figure 6. Observed (crosses), calculated (solid line), and difference (bottom) NPD Rietveld profiles for Sr_2CaIrO_6 at 2 K collected at the D1B-ILL diffractometer. The first series of Bragg reflections corresponds to the main perovskite phase, the second one corresponds to the vanadium used as a sample holder, and the third one corresponds to the magnetic structure.

versibilities, frustration, or freezing of the magnetic moments prevent the establishment of a perfect long-range ordering in this material.

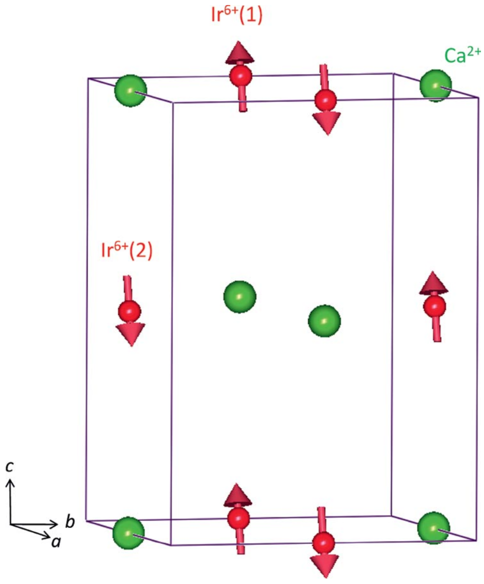

Figure 7. Schematic view of the magnetic structure of Sr_2CaIrO_6 below T_N.

For Sr_2MgIrO_6, no differences have been observed between the high- and low-temperature neutron diffraction patterns (Figure 5, b). Therefore, there is no long-range magnetic ordering detectable by NPD. The reason for this could be the small value of the magnetic moment (below the detection limit of the neutron diffraction) or the freezing of the moments because of the above-mentioned frustration effects in relationship with the large divergence between the ZFC and FC curves.

X-ray Absorption Measurements

The $L_{2,3}$ edges of transition-metal (T) compounds manifest very intense “white line” (WL) features owing to dipole transitions into final d states. The intensity, chemical shift, and spectral distribution of the WL features can provide information on the valence/T-d-orbital occupancy and the energy distribution of unoccupied density of states in transition-metal compounds.[19,20] Figure 8 shows the Ir L_3 edges of Sr_2MIrO_6 with M = Mg, Ca. For comparison, the spectra of the double perovskite with M = Sc along with those of elemental Ir and IrO_2 have also been measured and are included in Figure 8. The area of the WL feature in the Ir^{4+} IrO_2 standard is greatly enhanced and is chemically shifted to a higher energy relative to that of the elemental Ir standard. Both of these observations are consistent with a higher valence/d-hole count of the oxide. Similarly, relative to the Ir^{4+} IrO_2 standard, the Sr_2ScIrO_6 spectrum has a greater WL feature area and it is at higher energy supporting its Ir^{5+} d^4 ($2t_{2g}$ hole) configuration. The Sr_2CaIrO_6 spectrum is quite similar to that of the M = Sc compound but with an additional chemical shift to higher energy and the WL area increases motivated by the Ir^{6+} d^3 ($3t_{2g}$ hole) configuration of the M = Ca compound. The unresolved, bimodal WL structure of the M = Sc and Ca spectra will be discussed at greater length below. The Sr_2MgIrO_6 spectrum, shown in Figure 8, manifests a clear chemical shift of the WL feature to higher energy relative to that of the M = Sc spectrum but below that of Ca and supports the expected admixture of Ir^{6+} d^3 ($3t_{2g}$ hole) and Ir^{5+} d^4 ($2t_{2g}$ hole) configurations associated with the Mg compound. However, the even larger chemical shift of the Ca compound (from the next row down in the periodic Table) emphasizes that solid-state ligand-field splittings and bandwidth effects can lead to substantial variations in the WL structure and chemical shift.

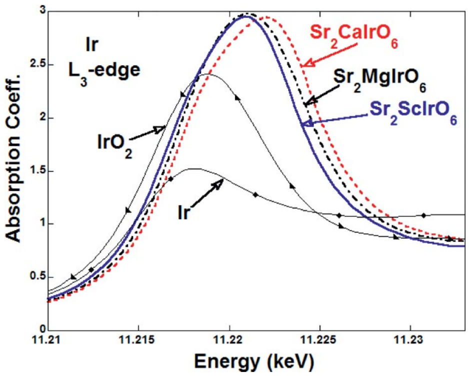

Figure 8. The Ir L_3 edges of Sr_2MIrO_6 with M = Mg, Ca, and Sc along with those of elemental Ir and IrO_2.

The proximity of Ca and Sc in the periodic table motivates a more detailed comparison of their double perovskite Ir L_3 spectral shape (i.e., their A–B feature structure) as shown in Figure 9. A more detailed description of the meaning of A and B features in perovskite oxides is incorporated in the Supporting Information (Figure S2). The M = Ca, Ir^{6+} d^3 ($3t_{2g}$ hole) spectrum in Figure 9 includes a prominent A-feature shoulder on the low-energy side of the B-feature peak. By comparison, the A feature in the M = Sc, Ir^{5+} d^4 ($2t_{2g}$ hole) spectrum is a less intense/prominent. For the spectral comparison in Figure 9, the Sc spectrum

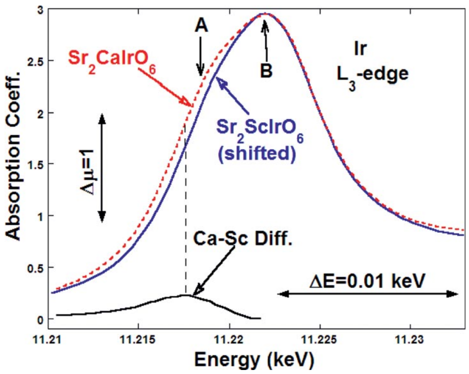

Figure 9. A superimposed comparison of the Ir L_3 edges of the Sr_2MIrO_6 (M = Ca and Sc) compounds. Here, the spectrum of the Sc compound has been displaced to higher energy until its e_g hole, B-peak feature coincides with that of the Ca spectrum.

was shifted up in energy until its B feature coincided with that of the Ca spectrum. A spline fit interpolation of the shifted M = Sc spectrum was then subtracted from the M = Ca spectrum to extract the Ca–Sc difference spectrum, which is also plotted in Figure 9. Here, this difference spectrum is intended to illustrate the distribution of excess t_{2g} hole states in the A feature in the Ca compound. Thus, although the A-feature intensity decreases with increasing t_{2g} electron occupancy is more subtle in the Ir compounds of Figure 9 than it was in the almost empty d-orbital cases illustrated in Figure S2, the effect is still clearly discernible.

Conclusions

Sr_2CaIrO_6 and Sr_2MgIrO_6 oxides with a perovskite-related structure have been synthesized under oxygen pressure conditions. The structural refinement from room-temperature NPD data was performed in the monoclinic $P2_1/n$ space group. The magnetic measurements show a transition to an antiferromagnetic ordering at Néel temperatures (T_N) of ca. 58 and 74 K, respectively. The effective magnetic moments calculated from the linear fit of the Curie–Weiss law at high temperatures indicate the presence of Ir^{6+} ions and also the absence of spin–orbit coupling for M = Ca and an admixture with Ir^{5+} ions for M = Mg; this is related to the oxygen understoichiometry determined for this oxide by NPD. The magnetic structure of Sr_2CaIrO_6 compound is defined by the propagation vector k = (1/2 1/2 0) and the arrangement for the Ir^{6+} magnetic moments have been defined as $m_{1x} = –m_{2x}$ and $m_{1z} = –m_{2z}$; for M = Mg, no long-range magnetic ordering is detected by NPD. X-ray absorption measurements for the Ir L_3 edges of Sr_2MIrO_6 with M = Mg and Ca compared with the double perovskite for M = Sc clearly show a Ir^{6+} d^3 ($3t_{2g}$ hole) configuration of the M = Ca compound, whereas for Sr_2MgIrO_6, the chemical shift of the WL feature to higher energy relative to the M = Sc spectrum but below that of Ca supports the expected admixture of Ir^{6+} d^3 ($3t_{2g}$ hole) and Ir^{5+} d^4 ($2t_{2g}$ hole) configurations.

Experimental Section

Sr_2CaIrO_6 and Sr_2MgIrO_6 were prepared by the citrate–nitrate method by using wet chemistry procedures. Stoichiometric amounts of $Sr(NO_3)_2$, IrO_2, and $CaCO_3$ or MgO, respectively, were dissolved in an aqueous citric acid solution with HNO_3 (1 mL). IrO_2 was not dissolved in the solution but stayed in suspension under magnetic stirring. This suspension was slowly evaporated to afford organic resins that contain a homogeneous distribution of the involved cations. After evaporation, the resulting resins were dried at 140 °C and then heated at 600 °C for 12 h to decompose the organic materials and eliminate the nitrate ions. Sequential annealing treatments in an oxidizing atmosphere were necessary to obtain these perovskite oxides as pure phases, owing to the presence of Ir^{6+} ions. In both samples, the obtained precursor powders were ground and heated at 800 °C in a O_2 flow for 12 h and then reground and heated at 950 °C under high oxygen pressure (200 bar) for 12 h for Sr_2CaIrO_6 and at 800 °C under 200 bar of oxygen for 36 h for Sr_2MgIrO_6. The reaction progress was followed after each treatment by X-ray diffraction (XRD) by using a Bruker-AXS D8 diffractometer (40 kV, 30 mA) controlled by the DRIFFACT^{PLUS} software in Brag–Brentano reflection geometry with Cu-K_α radiation (λ = 1.5418 Å) and a position-sensitive detector (PSD).

To study the crystallographic structures, NPD patterns were collected at room temperature with the high-resolution D2B diffractometer (λ = 1.594 Å) of the Institute Laue–Langevin (ILL) in Grenoble. To analyze the thermal evolution of the crystallographic structures as well as the eventual existence of a magnetic structure at low temperatures, NPD data were acquired in the temperature range from 2 to 100 K with the D1B instrument (λ = 2.52 Å). The crystal structures were refined from NPD data by the Rietveld method[21] by using the FULLPROF refinement program.[22] A pseudo-Voigt function was chosen to generate the line shape of the diffraction peaks. No regions were excluded in the refinement. The following parameters were refined in the final runs: scale factor, background coefficients, zero-point error, pseudo-Voigt corrected for asymmetry parameters, positional coordinates, and isotropic displacement.

The magnetic properties were studied with a commercial superconducting quantum interference device (SQUID) magnetometer from Quantum Design. The magnetic susceptibility was measured both in zero-field-cooled (ZFC) mode and field-cooled (FC) mode in the $4 \leq T \leq 400$ K range under an applied magnetic field of 0.1 T. Isothermal magnetization curves were obtained for magnetic fields from –5 to 5 T at 4 and 300 K.

The X-ray absorption spectroscopy (XAS) measurements were made in both fluorescence and transmission modes with the X-19A beamline at the National Synchrotron Light Source (NSLS) at Brookhaven National Laboratory by using a Si(111) double-crystal monochromator. A simultaneous standard was run with all the spectra. The data were processed with the standard linear pre- and post-edge background subtraction. By convention, the absorption coefficient (μ) is normalized to 1.0 over an average energy region well above the edge. To compare the samples of Sr_2CaIrO_6 and Sr_2MgIrO_6 with related compounds, Sr_2ScIrO_6 was prepared by a two-step procedure. Firstly, precursor powders were synthesized by a citrate route, and in a second step, the powders were heated at 800 °C in an O_2 flow for 12 h and then reground and heated at 1100 °C for 12 h.

Supporting Information (see footnote on the first page of this article): NPD patterns of Sr_2MgIrO_6 refined in the $P2_1/n$ and $I4/m$ space groups, L_3 edges of a series of d0/d1 double perovskite Ta, W, and Re compounds.

Acknowledgments

The authors thank the Spanish Ministry of Science and Technology (project number MAT2010-16404) and the Comunidad de Madrid (QUIMAPRES project number S2009PPQ-1551) for financial support. Dr. M. García-Hernández is thanked for the magnetic measurements and the authors are grateful to the Institut Laue–Langevin (ILL) for making all facilities available. Use of the National Synchrotron Light Source, Brookhaven National Laboratory was supported by the U.S. Department of Energy, Office of Science, Office of Basic Energy Sciences, under contract number DE-AC02-98CH10886.

---

[1] A. V. Powell, J. G. Gore, P. D. Battle, *J. Alloys Compd.* **1993**, *201*, 73.

[2] S. J. Moon, M. W. Kim, K. W. Kim, Y. S. Lee, J.-Y. Kim, J.-H. Park, B. J. Kim, S.-J. Oh, S. Nakatsuji, Y. Maeno, I. Nagai, S. I. Ikeda, G. Cao, T. W. Noh, *Phys. Rev. B* **2006**, *74*, 113104.

[3] M. Bremholm, S. E. Dutton, P. W. Stephens, R. J. Cava, *J. Solid State Chem.* **2011**, *184*, 601.

[4] J. P. Clancy, N. Chen, C. Y. Kim, W. F. Chen, K. W. Plumb, B. C. Jeon, T. W. Noh, Y.-J. Kim, *Phys. Rev. B* **2012**, *86*, 195131.

[5] D.-Y. Jung, G. Demazeau, J. H. Choy, *J. Mater. Chem.* **1995**, *5*, 517.

[6] T. K. Mandal, C. Felser, M. Greenblatt, J. Kübler, *Phys. Rev. B* **2008**, *78*, 134431.

[7] D.-Y. Jung, G. Demazeau, *J. Solid State Chem.* **1995**, *115*, 447.

[8] D.-Y. Jung, G. Demazeau, G. Etourneau, *J. Mater. Res. Bull.* **1995**, *30*, 113.

[9] D.-Y. Jung, P. Gravereau, G. Demazeau, *Eur. J. Solid State Inorg. Chem.* **1993**, *30*, 1025.

[10] I. Qasim, B. J. Kennedy, M. Avdeev, *J. Mater. Chem. A* **2013**, *1*, 13357.

[11] I. Qasim, B. J. Kennedy, M. Avdeev, *J. Mater. Chem. A* **2013**, *1*, 3127.

[12] M. Bremholm, C. K. Yim, D. Hirai, E. Climent-Pascual, Q. Xu, H. W. Zandbergen, M. N. Ali, R. J. Cava, *J. Mater. Chem.* **2012**, *22*, 16431.

[13] R. D. Shannon, *Acta Crystallogr., Sect. A* **1976**, *32*, 751.

[14] P. M. Woodward, *Acta Crystallogr., Sect. B* **1997**, *53*, 32.

[15] J. H. Choy, D. K. Kim, S. H. Hwang, G. Demazeau, D. Y. Jung, *J. Am. Chem. Soc.* **1995**, *117*, 8557.

[16] P. D. Battle, G. R. Blake, T. C. Gibb, J. F. Vente, *J. Solid State Chem.* **1999**, *145*, 541.

[17] S. J. Mugavero, M. D. Smith, H. C Zur Loye, *J. Solid State Chem.* **2005**, *178*, 200.

[18] M. Walewski, B. Buffat, G. Demazeau, F. Wagner, M. Pouchard, P. Hagenmuller, *Mater. Res. Bull.* **1983**, *18*, 881.

[19] G. Popov, M. Greenblatt, M. Croft, *Phys. Rev. B* **2003**, *67*, 024406.

[20] Q. Lin, M. Greenblatt, M. Croft, *Pol. J. Soil Sci. J. Solid State Chem.* **2005**, *178*, 1356.

[21] H. M. Rietveld, *J. Appl. Crystallogr.* **1969**, *2*, 65.

[22] J. Rodríguez-Carvajal, *J. Phys. B* **1993**, *192*, 55.

Received: August 21, 2013